**Supporting information**

# Multicycle Operando Raman Spectroscopy Reveals Reversible and Irreversible Transitions in $LiNiO_2$ Electrodes

*Eva del Campo Ortiz*[a], *Alex R. Neale*[b], *Manel Sonni*[c,d], *Luke M. Daniels*[c,d], *Grazyna Zofia Zukowska*[a], *Matthew J. Rosseinsky*[c,d], *Marek M. Marcinek*[a]*, *Laurence J. Hardwick*[b,d]*.

[a] Faculty of Chemistry, Warsaw University of Technology, Noakowskiego 3, 00-664 Warsaw, Poland

[b] Stephenson Institute for Renewable Energy. Department of Chemistry, University of Liverpool, Liverpool, L69 7ZD, United Kingdom

[c] Materials Innovation Factory, Department of Chemistry, University of Liverpool, Liverpool, L69 7ZD, United Kingdom

[d] The Faraday Institution, Quad One, Harwell Science and Innovation Campus, Didcot OX11 0RA, United Kingdom

**Characterisation of synthesised $LiNiO_2$**

**Table S1.** ICP-MS analysis of $LiNiO_2$.

| Target composition | ICP-MS composition |
|---|---|
| $LiNiO_2$ | $Li_{1.019(20)}Ni_{1.000(27)}O_2$ |

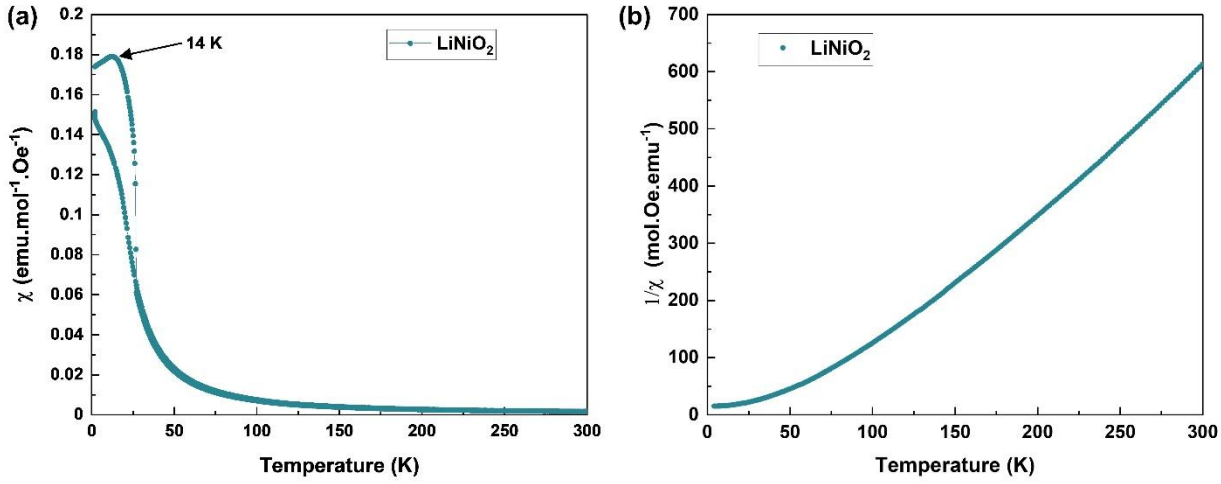


**Figure S1.** (a) Zero-Field cooled (ZFC), and field-cooled (FC) magnetic susceptibility data collected under an applied field of 100 Oe for $LiNiO_2$. The magnetic freezing temperature ($T_f$) of 14 K is determined from the maxima of the ZFC curve. (b) FC reciprocal magnetic susceptibility collected under an applied field of 45 kOe for $LiNiO_2$.

## Operando Raman cell

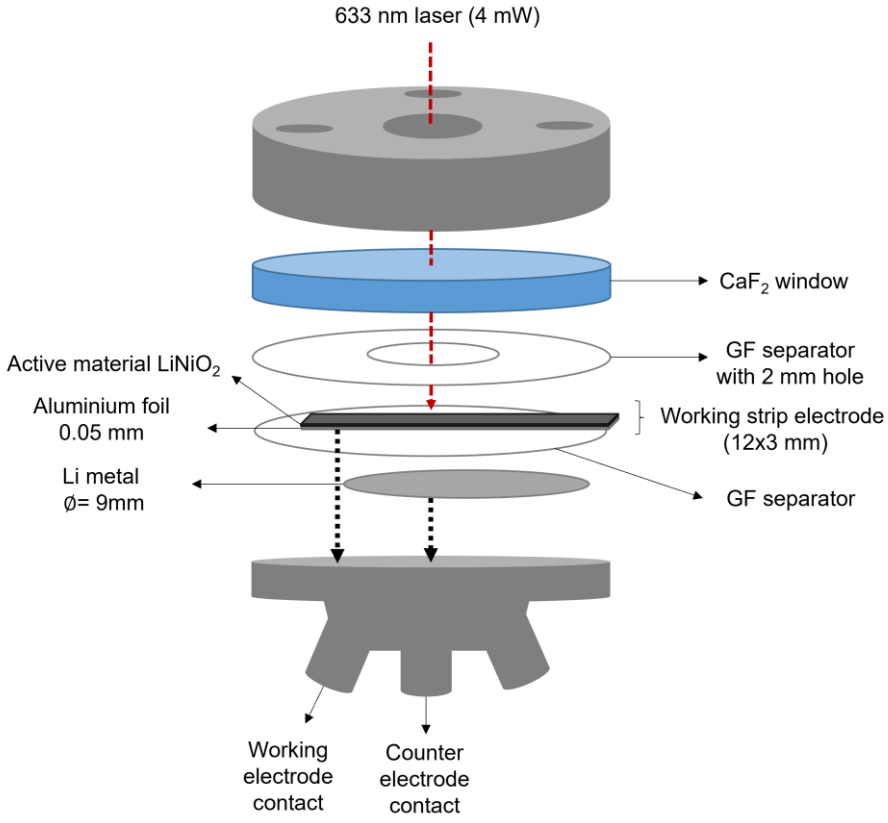


**Figure S2.** Schematic representation of operando Raman cell. The assembly comprises two glass fibre separators embedding the composite working electrode.

**Electrode fabrication**

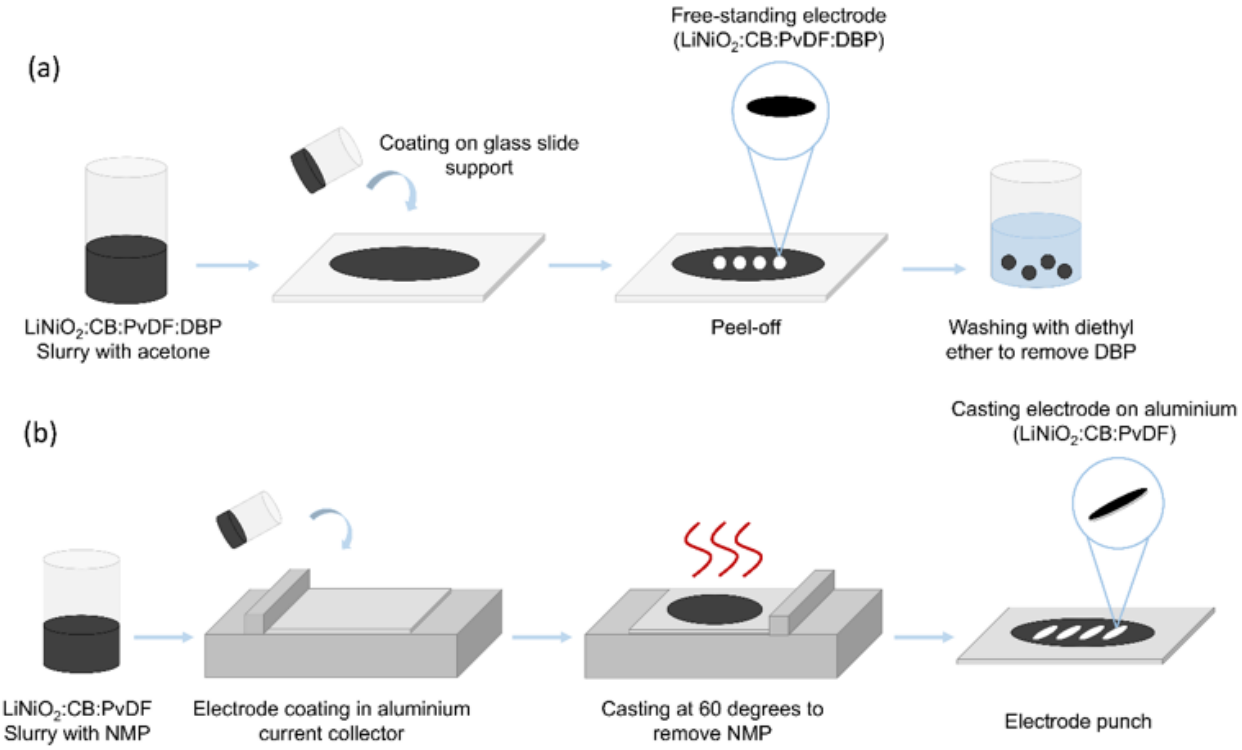


**Figure S3**: (a) Free standing and (b) strip electrode preparation. Once the electrodes were punched out, they were dried under vacuum at 90 °C, weighed and then transferred to an argon filled glovebox ($O_2$, $H_2O$ < 1 ppm) prior to Raman cell assembly.

**Free standing electrode formulation**

$LiNiO_2$, carbon black (CB) (Super P), poly(vinylidene difluoride- (PVDF) and dibutyl phthalate (DBP, Aldrich) were dispersed in acetone and then cast onto glass at a thickness of 60 µm. Once dry, the free-standing film was removed from the glass plate with the dibutyl phthalate plasticiser extracted using diethyl ether, leaving a porous film ca. 50 µm thick, which was cut into 6 mm diameter electrodes.

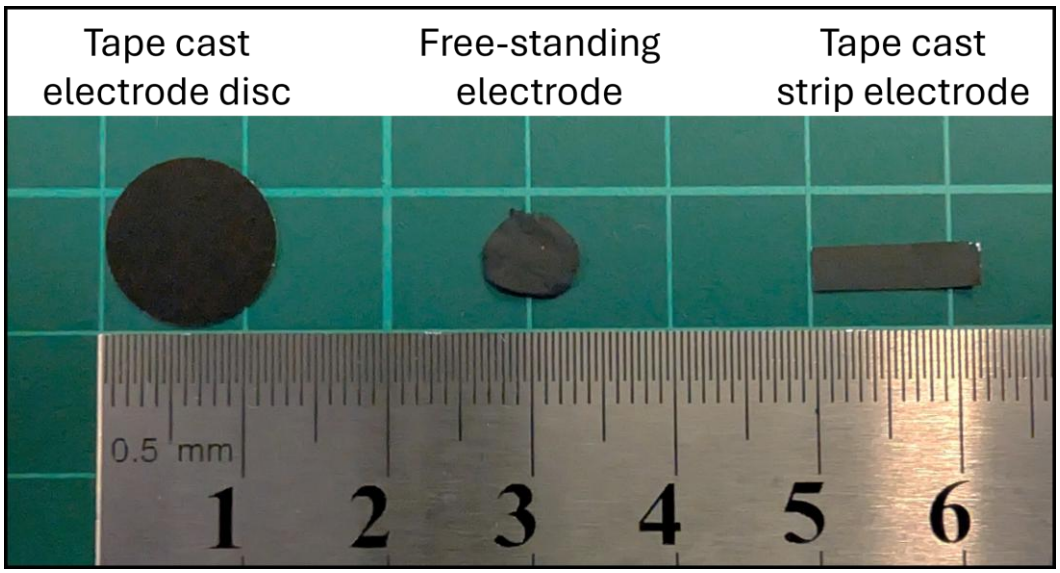


**Figure S4**. Comparison of the various utilised electrodes for electrochemical and operando Raman measurements.

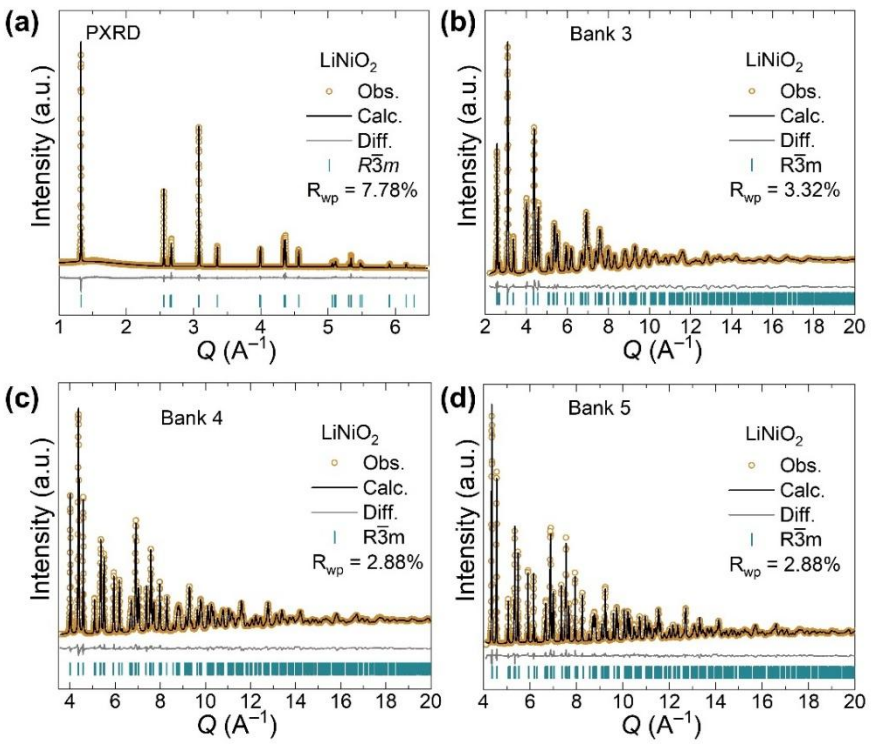


**Figure S5.** Combined Rietveld refinement of $^{7}LiNiO_2$ against (a) powder XRD and time-of-flight neutron powder diffraction (NPD) data collected from (b) Bank 3 ($2\theta = 67°$), (c) Bank 4 ($2\theta = 122°$), and (d) Bank 5 ($2\theta = 154°$) of NOMAD at room temperature using the multidomain single-phase hexagonal $R\bar{3}m$ model described in the main text. Traces $I_{obs}$ (blue circles), $I_{calc}$ (black line), $I_{obs}-I_{calc}$ (grey line), and Bragg reflections (orange tick marks) are shown. The combined refinement including XRD data and NPD data across four detector banks has an $R_{wp}$ of 3.08%, $R_{exp}$ of 0.38%, and GoF of 8.06.

**Table S2.** Fractional atomic coordinates and isotropic displacement parameters of $^{7}LiNiO_2$. The combined refinement including XRD data and NPD data across three detector banks has an $R_{wp}$ of 3.08%, $R_{exp}$ of 0.38%, and GoF of 8.06. A chemical order parameter, which is defined as the difference in Li content between the two distinct cation (Li and Ni) layers via $\eta = |occ_{Li} - occ_{Ni}|$, of 0.95(3) is extracted from the refinement indicating a low degree of cation mixing.

| $R\bar{3}m$ : $a$ = 2.879048(14) Å, $c$ = 14.20017(13) Å, $V$ =100.935(2) Å$^3$ | | | | | | |
|---|---|---|---|---|---|---|
| **Atom** | **Wyck.** | **S.O.F.** | ***x*** | ***y*** | ***z*** | **$B_{iso}$ (Å$^2$)** |
| Li1 | 3*b* | 0.9764(5) | 0.00000 | 0.00000 | 0.00000 | 0.83(2) |
| Ni1 | 3*b* | 0.0236(5) | 0.00000 | 0.00000 | 0.00000 | 0.83(2) |
| Li2 | 3*a* | 0.0236(5) | 0.00000 | 0.00000 | 0.50000 | 0.241(2) |
| Ni2 | 3*a* | 0.9764(5) | 0.00000 | 0.00000 | 0.50000 | 0.241(2) |
| O | 6*c* | 1 | 0.00000 | 0.00000 | 0.24119(2) | 0.757(5) |

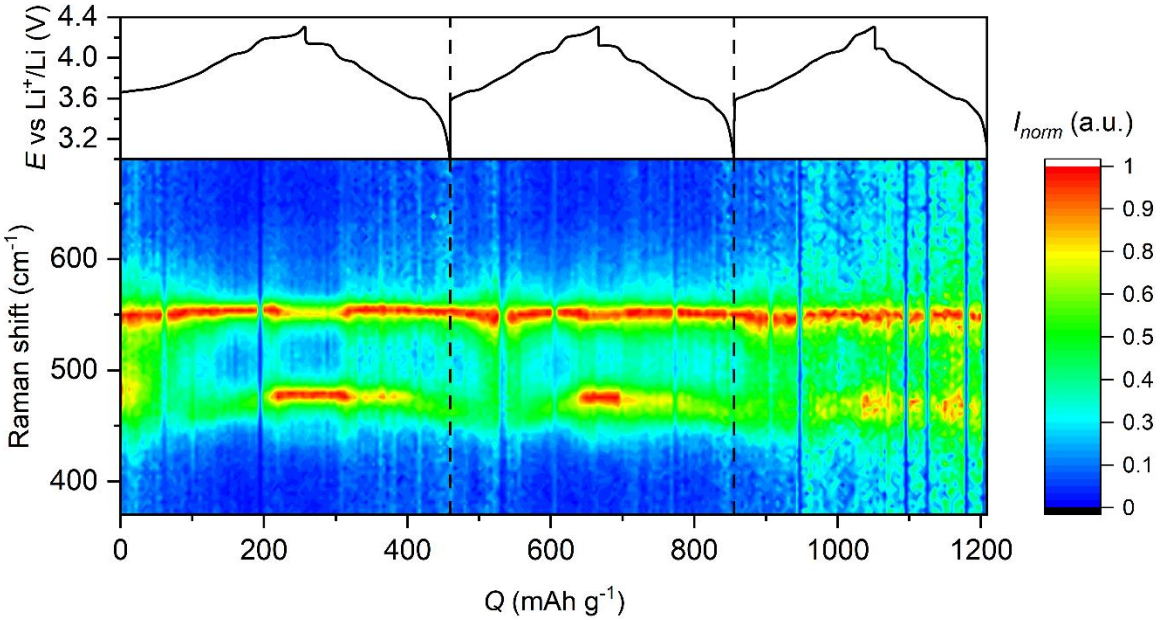


**Figure S6**. Operando Raman spectra series for the first three cycles of the $LiNiO_2$ tape cast electrode strip, at C/10 rate displayed as spectral band intensity heat map against galvanostatic cycling potential profiles.

**Origin *vs* PRISMA Raman data treatment**

A key challenge in operando experiments is the individual deconvolution of each spectrum to recognize the changes occurring in the characteristic modes of $LiNiO_2$. **Figure S5** shows how from a single spectrum, four types of plots could be obtained giving information about peak position and peak intensity for both $E_g$ and $A_{1g}$ modes. **Figure S5** depicts an Origin-derived spectrum deconvolution, along with scatter plots for certain potential values during the first cycle of $LiNiO_2$.

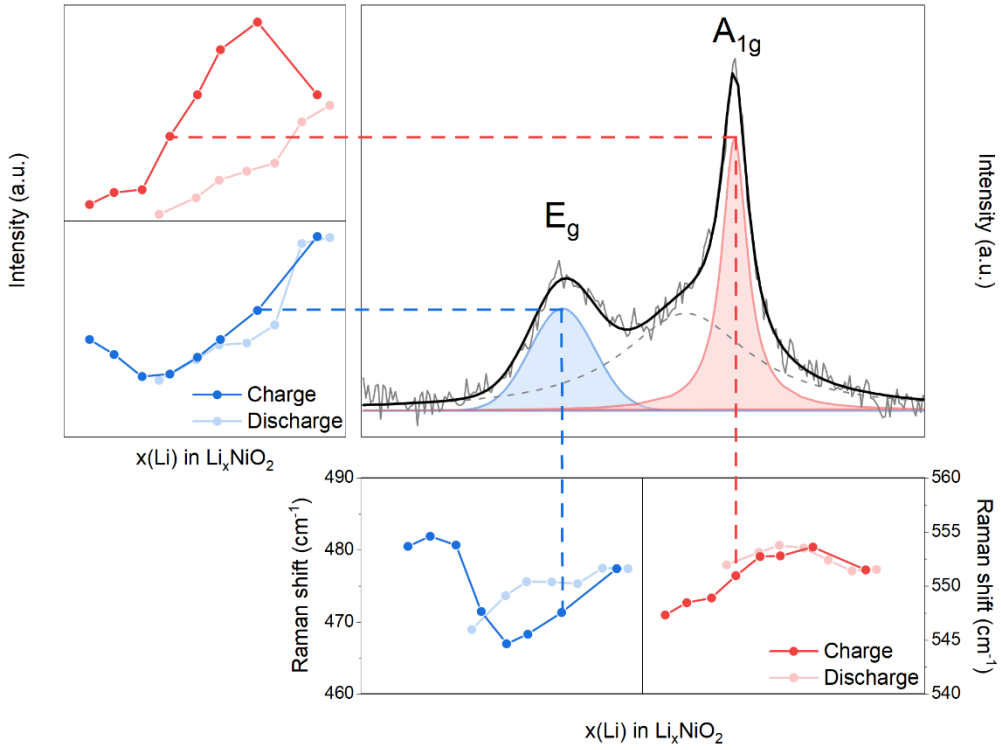


**Figure S7**. Origin manual deconvolution for the first cycle of $LiNiO_2$ tape cast electrode strip in EL-Cell obtaining peak position and intensity data for $E_g$ and $A_{1g}$ modes. The grey, dash trace corresponded to an electrolyte band (dimethyl carbonate) observed at 520 $cm^{-1}$.

Other prominent electrolyte bands were located away from the $LiNiO_2$ signals in the 700 $cm^{-1}$ and 900 $cm^{-1}$ regions, all corresponding to the electrolyte solvent bands.[1] During potential cycling no major change in the electrolyte Raman signals were observed.[2]

Analysis *via* Origin software of a selected electrode sample from the total collected data for the first cycle took approximately five hours. For comparison, use of PRISMA took only five minutes to analyse the whole spectral dataset, thereby reducing the processing time for the evaluation of the whole experiment, since the data process is carried out in batch automatically.[3] In **Figure S6** the comparison between the deconvolution analyses using Origin and using the PRISMA app is shown. Data derived from both Origin and PRISMA fitting methods followed similar trends in peak shift position and intensity, with only minor discrepancies observed between the two methods.

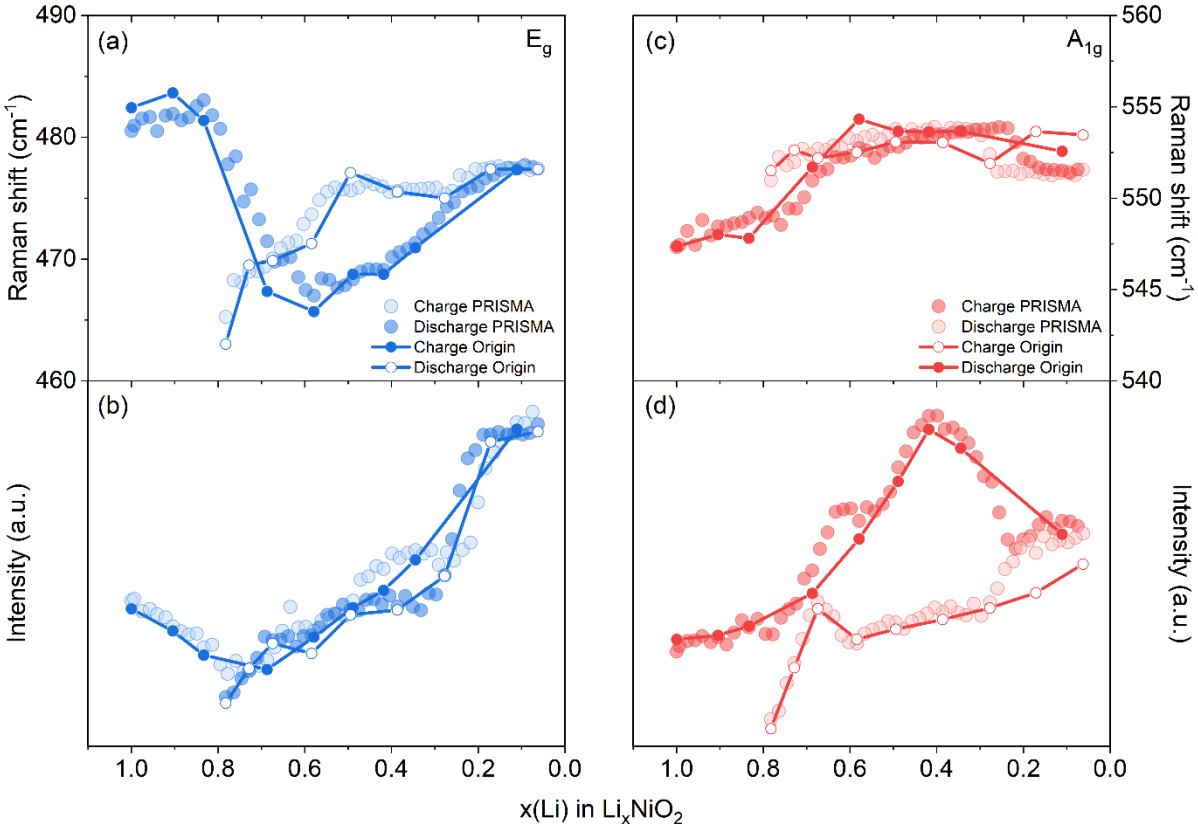


**Figure S8**. Comparison between Origin manual deconvolution and PRISMA app batch analysis for $E_g$ peak position (a) and intensity (b) and $A_{1g}$ peak position (c) and intensity (d) for the first cycle of $LiNiO_2$ tape cast electrode strip. Origin deconvolution is represented with dots jointed by lines while PRISMA results are represented only by dots. The different colour tonalities represent charge and discharge trends.

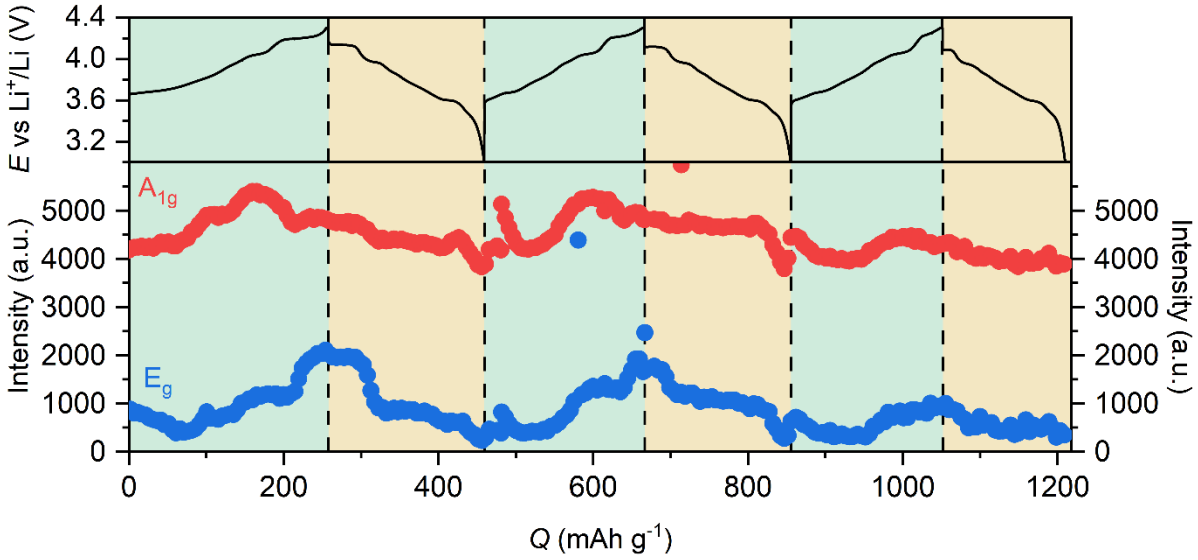


**Figure S9**. Intensity data before normalisation for both $E_g$ and $A_{1g}$ characteristic modes for three cycles. Outlier values can be seen arise from incorrect deconvolution by PRISMA triggered via noise spikes (from cosmic rays) local to the band positions.

Discontinuities in band intensity at ca. 470 and 850 mAh $g^{-1}$ arise either from refocusing the objective onto the electrode surface or result from the potential difference of switching polarity of the current. Normalisation of the intensities between cycle to cycle may exaggerate these intensity jumps (as seen in Figure 3).

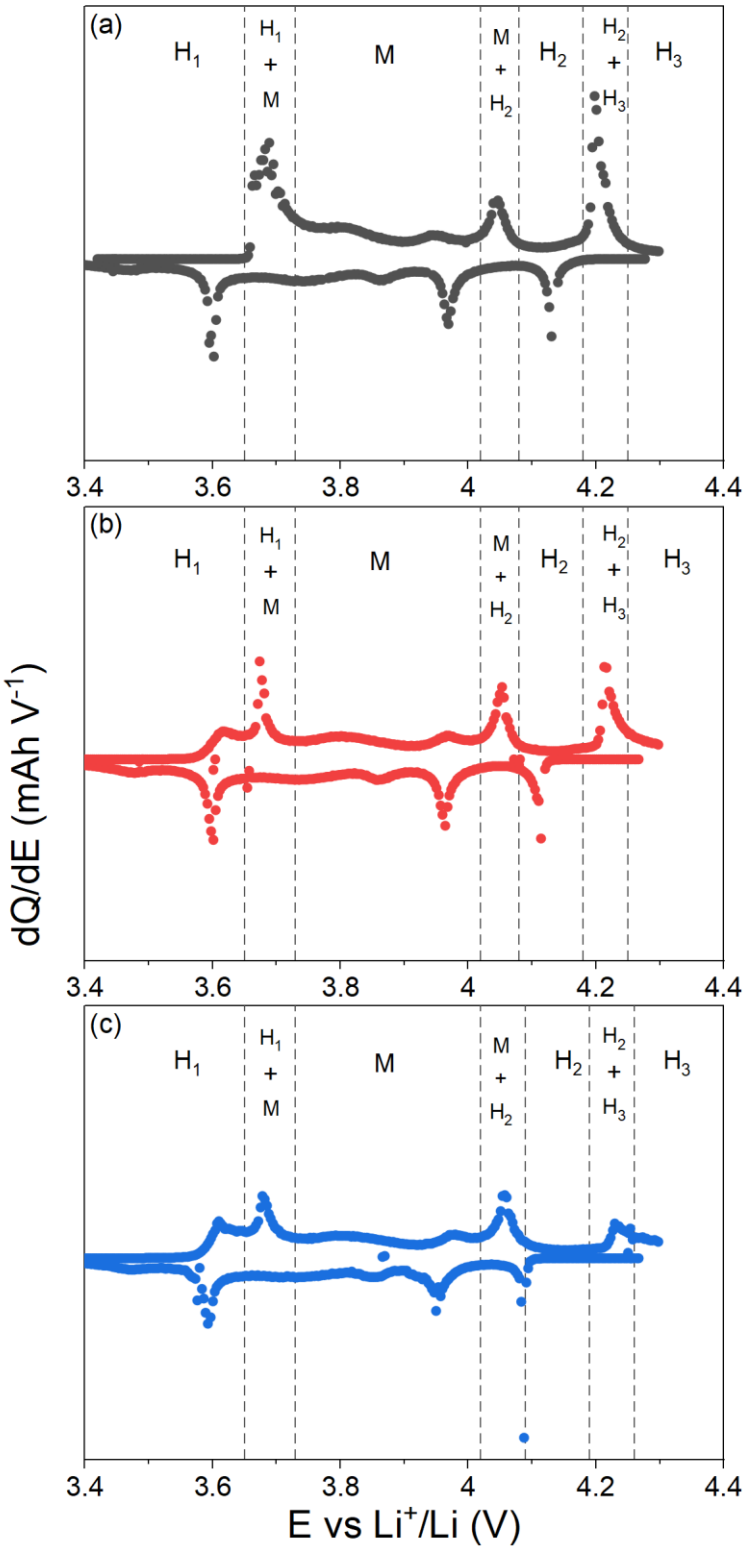


**Figure S10.** Differential capacity (dQ/dE) *vs*. E (V *vs.* $Li^+/Li$ ) for (a) cycle 1, (b) cycle 2, and (c) cycle 3 of the $Li_xNiO_2$ tape-cast electrode in the operando Raman cell. The different phase transition regions for $LiNiO_2$ during the charge step of each cycle are indicated, corresponding to the potential ranges in **Table 1** in the main text.

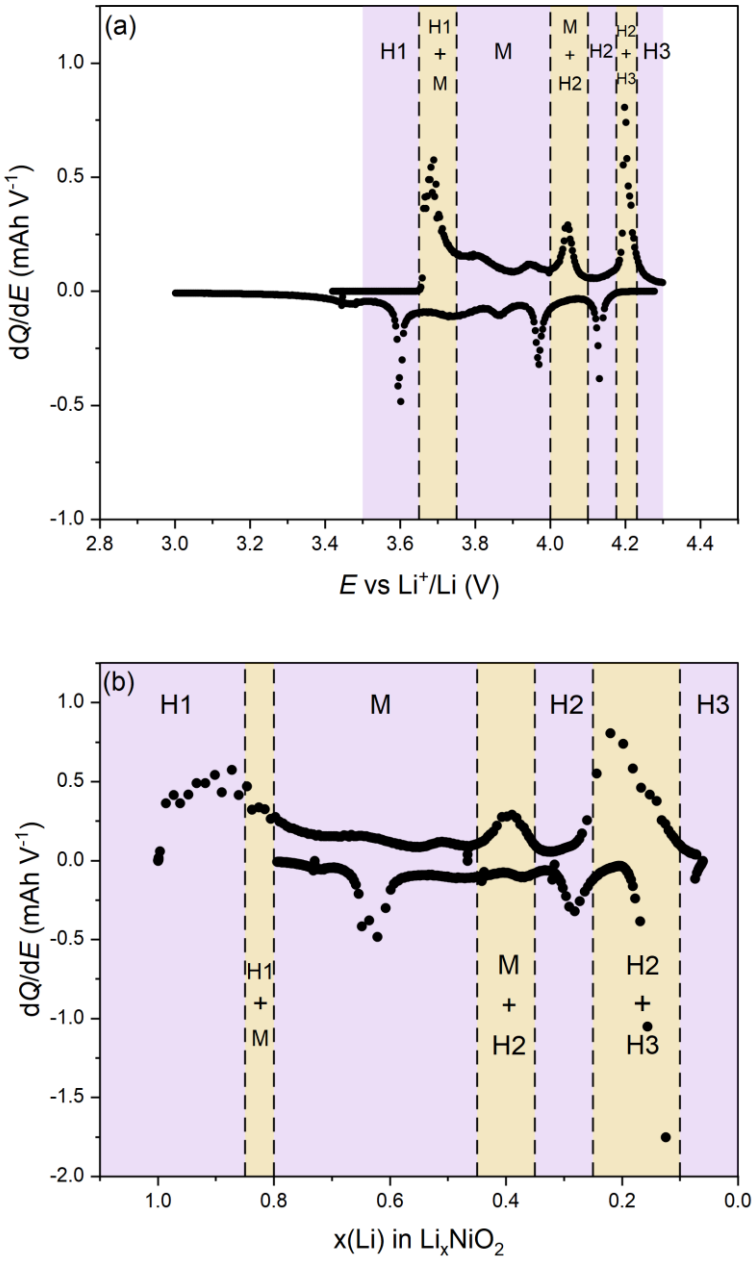


**Figure S11.** Differential capacity (dQ/dE) *vs*. (a) E *vs*. $Li^+$/Li (V) and (b) *x*(Li) in $Li_xNiO_2$. The different phase transition regions for $LiNiO_2$ during the first cycle charge, are indicated by the coloured rectangles.

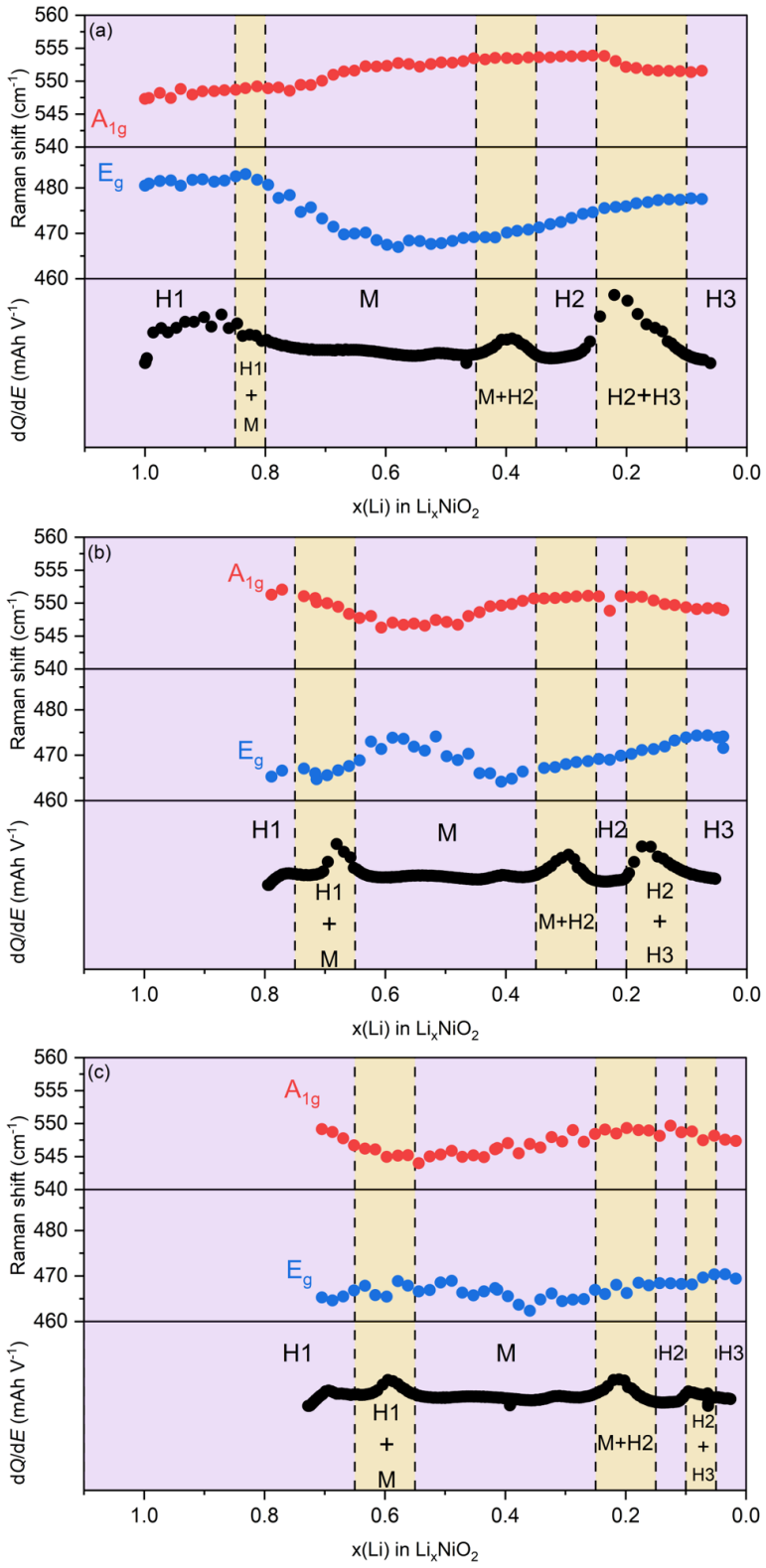


**Figure S12.** Peak position trends for $E_g$ and $A_{1g}$ bands for the charge of the initial three cycles plotted with the differential capacity *vs*. x(Li) in $Li_xNiO_2$ for (a) cycle 1, (b) cycle 2, and (c) cycle 3.

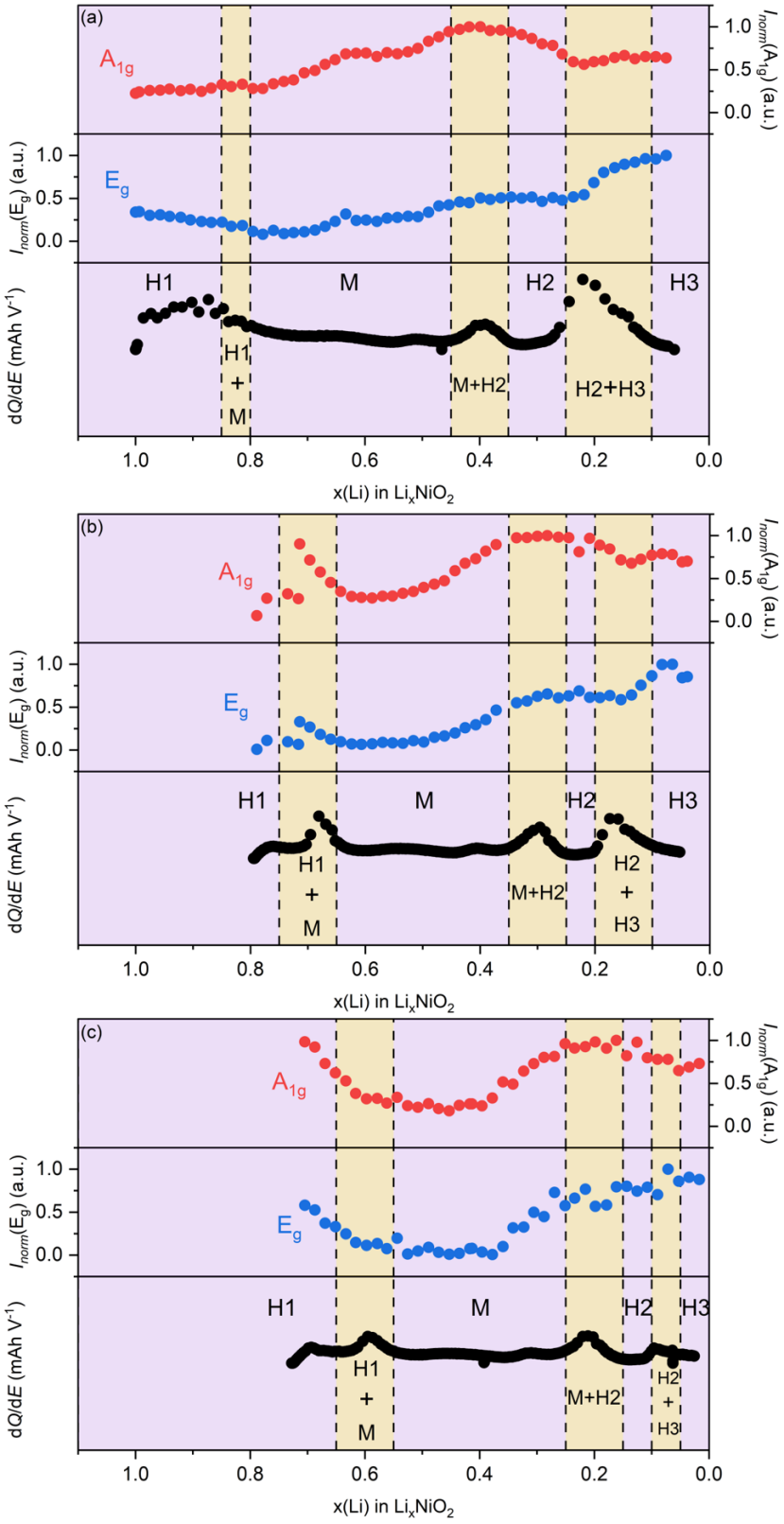


**Figure S13.** Peak intensity variation for $E_g$ and $A_{1g}$ bands during the charge of the initial three cycle plotted with the differential capacity *vs*. x(Li) in $Li_xNiO_2$ for (a) cycle 1, (b) cycle 2, and (c) cycle 3.

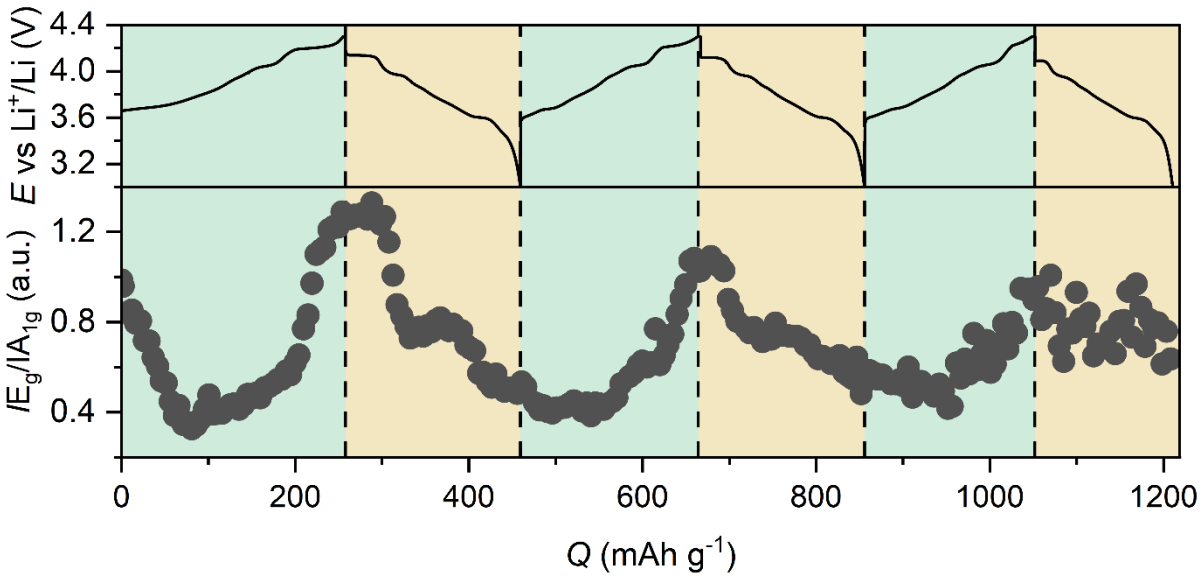


**Figure S14.** Relative band intensities for the $E_g$ and $A_{1g}$ modes (*i.e.*, $I_{Eg}/I_{A1g}$) along the initial three lithiation and delithiation cycles of $LiNiO_2$.

## REFERENCES


(1) Heber, M.; Hofmann, K.; Hess, C. Raman Diagnostics of Cathode Materials for Li-Ion Batteries Using Multi-Wavelength Excitation. *Batteries* **2022**, *8* (2). https://doi.org/10.3390/batteries8020010.

(2) Chen, Z.; Kang, S.; Peng, J.; Cai, Y.; Huang, Y.; Pan, Q.; Zheng, F.; Wang, H.; Li, Q.; Hu, S. Capturing Oxygen-Driven Electrolyte Oxidation during High-Voltage Cycling in Li-Rich Layered Oxide Cathodes. *ACS Energy Lett.* **2023**, *8* (1), 417–419. https://doi.org/10.1021/acsenergylett.2c02509.

(3) Flores, E.; Mozhzhukhina, N.; Li, X.; Norby, P.; Matic, A.; Vegge, T. PRISMA: A Robust and Intuitive Tool for High-Throughput Processing of Chemical Spectra**. *Chem. Res.* **2022**, *2* (10), 1–9.